

UNCLASSIFIED

Defense Technical Information Center  
Compilation Part Notice

ADP012359

TITLE: Simulation of Cryogenic Jet Injection, RCM 1

DISTRIBUTION: Approved for public release, distribution unlimited

This paper is part of the following report:

TITLE: 2nd International Workshop on Rocket Combustion Modeling:  
Atomization, Combustion and Heat Transfer held in Lampoldshausen,  
Germany on 25-27 Mar 2001

To order the complete compilation report, use: ADA402618

The component part is provided here to allow users access to individually authored sections of proceedings, annals, symposia, etc. However, the component should be considered within the context of the overall compilation report and not as a stand-alone technical report.

The following component part numbers comprise the compilation report:

ADP012355 thru ADP012373

UNCLASSIFIED

# Simulation of Cryogenic Jet Injection, RCM 1

R. Branam\*, J. Telaar<sup>o</sup> and W. Mayer<sup>o</sup>

\*Air Force Research Laboratory, Edwards AFB  
German Aerospace Center (DLR), Space Propulsion Institute, Lampoldshausen

## Abstract

Understanding the complex environment of the rocket chamber involves good knowledge of the injection phenomena. Understanding the injection phenomena allows the rocket designer to employ time and cost saving modeling tools to design a higher performance rocket engine. The rocket engine performance is highly dependent on the injection processes within the chamber. This project looked at injection processes in the supercritical régime of the injected fluid, cryogenic nitrogen, in order to better understand realistic conditions in the rocket engines of today. The investigation considered test conditions from 4.0 to 6.0 MPa at two different injection velocities and temperatures. For the RCM-1-A and RCM-1-B cases, the target test conditions are 5 m/s injection velocity and 120 K injection temperature. RCM-1-A is at 4 MPa and RCM-1-B is at 6 MPa. Experimental data taken by Raman imaging and Shadowgraphy were compared to computational models for these various test conditions. The test data allows comparisons of density, length scales and jet spreading angles. The results validate the computational models and agree with classical theory.

## Introduction

There is much interest in high pressure combustion for the production of high power energy conversion and thrust. This is found in diesel engines, gas turbines, and, in particular, rocket engines. These high pressures often exceed the critical pressures of the injected fuel and/or oxidizer. Understanding the complex environment of the rocket chamber in order to get the most power out of it requires a good understanding of the injection phenomena. This understanding allows the rocket designer to employ time and cost saving modeling tools to better design a higher performing rocket engine. Much work has been accomplished in this area as can be seen in references <sup>1, 2, 3</sup> and <sup>4</sup>, but a strong understanding of the injection process and the development of reliable modeling tools still requires much work. This work takes a step in this direction by looking at cryogenic injection at pressures above the critical pressure and modeling of this flow<sup>5</sup>. A more complete discussion of this effort including further testing conditions can be found in reference <sup>6</sup>. The comparison between measured and calculated values provides some insight as to the reliability of the modeling effort and behavior above critical pressures.

## Problem

This investigation looks at the behavior and properties of a cryogenic, axisymmetric jet in a supercritical environment. The experiment injects liquid nitrogen above the

critical point (3.39 MPa) through a single injector into a chamber filled with ambient temperature gaseous nitrogen. The experimental conditions look at the effects of pressure, temperature and injection speed of the liquid nitrogen into the chamber. The targeted testing conditions are injection values of 5 m/s and 120 K and RCM-1-A, 4 MPa; RCM-1-B, 6 MPa. Actual injection conditions are determined from previous experiments to determine temperature variation along the injector tube and calculated in the computational models based on these experiments. At these conditions, Raman and Shadowgraph images were taken encompassing the area from the injector to 60 mm (approximately 30 injector diameters) from the injector. The pictures were used to determine density distributions, jet spreading angles and length scales. These measured values were compared to computational models for each of the cases.

## Cryogenic Jet

A jet flow has three distinct zones: potential core, development or transition region, and a similarity region as seen in Figure 1. The potential core contains some portion consisting of only injected fluid and reduces in thickness as the jet mixes with entrained fluid from the surrounding environment.

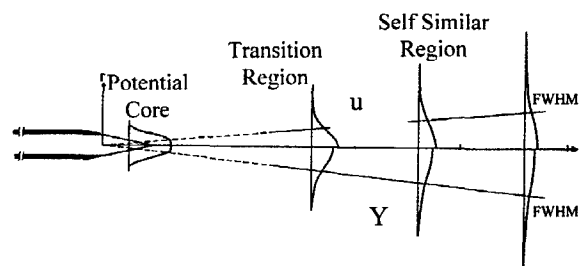


Figure 1: Jet mixing flow field

After the potential core region, the jet is in a transitional state which is considered the region of turbulent mixing for a jet. In this region, the energy dissipation and the jet behavior tend to be of the highest interest for mixing purposes. Researchers have indicated the most significant influences on jet development include the velocity ratio between initial jet velocity and the surrounding environment ( $u_0/u_\infty$ ) and the density ratio ( $\rho_0/\rho_\infty$ ). These parameters show how the momentum and thermal energy dissipates from the jet into the flow field.

At some distance from the injection plane, the jet becomes self similar. This means a function of only one variable can express the flow field profiles as no longer varying in the axial direction. Schetz<sup>7</sup> stated this to occur at approximately  $x/d \geq 40$ , while others have indicated for

similar jets, velocity profiles exhibit self similar behavior as close as  $x/d \geq 20$  (Schlichting<sup>8</sup>). Other parameters such as turbulence intensities ( $u'$ ,  $v'$ ,  $w'$ ) may not show this behavior until well after  $x/d \geq 200$ . Also, the particular variable employed to show self similar behavior varies between researchers.

### Incompressible Jet

At pressures above the critical pressure and near critical temperatures, changes in the temperature can correspond to extreme density gradients. For this reason, real gas effects must be taken into account when determining flow properties. Since pressure is relatively constant, this density gradient is only dependent on temperature. The experiment considers the density to be incompressible or weakly compressible according to the classical definition of compressibility. By using a real gas relationship for density, coefficient of specific heat at constant pressure and viscosity, the computational model captures the effects of being weakly compressible when employing an incompressible solution technique. This relationship also defines a very strong relationship between temperature and density. The expected results for temperature and density in radial and axial profiles in the flow field are related but the relationship is not linear.

### Turbulent Prandtl Number Considerations

Schetz<sup>7</sup> showed the value of the Prandtl number actually varies with radial location but on average is 0.7 for similar axisymmetric submerged jets. The evidence from Pabst<sup>9</sup> and Sakipov<sup>10</sup> calculated values ranging from 0.4 to 1.7 for various fluids and locations. Also, most modeling codes use values of 0.89 or 0.9 as the default value (Wilcox<sup>11</sup>, CFD ACE manual<sup>12</sup>). Values less than one correspond to thermal energy dissipating in the flow quicker than momentum energy due to turbulent mixing. The resulting non-dimensional temperature profiles would then be wider in comparison to the non-dimensional velocity profiles. According to White<sup>13</sup>, the value should be greater than 0.7 and suggests 0.9 or 1.0. Although this parameter varies over the radial profile of the flow, it is common to choose a constant value for the entire flow field. The solutions for RCM-1-A employed Prandtl number values of 1.0 (White) and 0.7 (Schetz) as defined by the following equation.

$$Pr_T = \frac{\nu_T}{\kappa_T / \rho c_p}$$

A constant value provided good results in these computational models. The results are further discussed later, but  $Pr_T = 1.0$  proved to be more consistent with our experimental density data and was used. It also allows the results to show thermal influences due to the changes in the coefficient of thermal heat transfer under these temperature and pressure conditions without large influences caused by numerically induced turbulent energy transfer.

### Property Value Comparisons

Non-dimensionalizing the flow properties for the radial profiles makes it possible to compare the data for the different testing conditions as follows.

$$\rho^* = \frac{\rho - \rho_c}{\rho_c - \rho_\infty} \quad u^* = \frac{u}{u_c}$$

The  $c$  subscript refers to the centerline or maximum value for the profile and the infinity designates the environmental values. By this method, the profiles are 1.0 at the centerline and zero outside the jet itself. Non-dimensionalizing length measurements uses the jet diameter ( $d$ ), Full Width Half Maximum (FWHM) values ( $r_{1/2}$ ), and axial location as indicated.

The results compare the property profiles at axial locations of  $x/d = 0, 1.2, 5, 10, 15, 20,$  and  $25$ . Measured values at  $x/d = 0$  are not possible due to the reflection of laser light at these locations. The flow properties are also compared and investigated in the axial direction. Density and velocity are of particular interest. These employ similar relationships to the radial comparisons with one difference. The non-dimensionalization of these parameters uses the injection conditions ( $\rho_\infty, u_\infty$ ) rather than the local centerline values as shown in the following equations.

$$\rho^* = \frac{\rho - \rho_\infty}{\rho_\infty - \rho_\infty} \quad u^* = \frac{u}{u_\infty}$$

### Jet Divergence Angle

The jet divergence angle seems to be one of the most highly considered parameters for jet flows. It lends itself to be easily measured and compared with other results. Chehroudi et. al.<sup>14</sup> provided a comparison of many different empirical models with available test data under various conditions. Of particular interest to this experiment were the models put forth by Dimotakis<sup>15</sup> and Papamoschou-Roshko<sup>16</sup>. Dimotakis investigated the entrainment of mass flow into the growing shear layer of a free jet. He proposed a vorticity growth rate equation seen below depending on velocity and density ratio between the fluid flows. For these testing conditions, the velocity ratio is zero, simplifying the following equation considerably.

$$\delta_m = 0.17 \left\{ \frac{\left(1 - \frac{u_\infty}{u_c}\right)}{\left[1 + \left(\frac{\rho_\infty}{\rho_c}\right)^{1/2} \left(\frac{u_\infty}{u_c}\right)\right]} \right\} \left\{ 1 + \left(\frac{\rho_\infty}{\rho_c}\right)^{1/2} - \frac{\left[1 - \left(\frac{\rho_\infty}{\rho_c}\right)^{1/2}\right]}{\left[1 + 2.9 \frac{(1 + u_\infty/u_c)}{(1 - u_\infty/u_c)}\right]} \right\}$$

Papamoschou and Roshko proposed a visual thickness equation for incompressible, variable-density mixing layers while studying the turbulence and compressibility effects in plane shear layers. This relationship uses a convective velocity definition to relate the difference in the flows. The experimentally determined constant (0.17) allows results to be compared with axisymmetric jet flows. Again, since the velocity ratio for this effort is zero, the relationship simplifies considerably.

$$\delta_m = 0.17 \left(1 - \frac{u_\infty}{u_c}\right) \frac{\left[1 + \left(\frac{\rho_\infty}{\rho_c}\right)^{1/2}\right]}{\left[1 + \left(\frac{u_\infty}{u_c}\right) \left(\frac{\rho_\infty}{\rho_c}\right)^{1/2}\right]}$$

Various methods could determine the spreading angle from the computational models. Direct evaluation of the edge of the shear layer using a 0.99 roll-off point for temperature, density, and velocity provides a simple

method to accomplish this task. This method can be compared with values determined using a FWHM approach. The edge of the shear layer is difficult to determine from Raman images, so the procedure determines the location of half the maximum value. The procedure is to multiply the value by two as suggested by Chehroudi et al.<sup>14</sup> to compare with visual techniques such as the results from the Shadowgraph images. A similar approach for the computational models also calculate FWHM values to use as a comparison for the Raman results. The Shadowgraph images allow direct determination of the angle. These pictures clearly show the edge of the shear layer.

### Experimental Setup

Figure 2 shows the pressurized chamber with the injector used in the experiments presented in this paper along with the boundary conditions assumed for the model. The diameter of the injector is 2.2 mm and the length to diameter ratio is greater than 40 (Figure 3). The chamber can be pressurized up to 6 MPa and is equipped with an electronic heater to keep the wall temperature constant. Optical access to the chamber is provided by four windows. Cold nitrogen is injected into a warm nitrogen environment under different ambient and injection conditions. The temperature of the injected fluid can vary from 100 to 140 K, the injection velocity ranges from 1 to 10 m/s, and the ambient pressure can be as high as 6 MPa.

The temperature of the injected fluid is generally measured at position 1 (T1, Figure 3). Since the test setup includes no temperature regulation system, the injection temperature is varied by starting the injection at the ambient temperature of the injector and the piping. During injection, the piping and the injector cool down while the injected fluid heats up. When the temperature of the injected fluid reaches its targeted value, the experiment records the Shadowgraph or Raman images. Since the time required to take the images is small compared to the time the injector needs to cool down, the project assumes quasi steady state conditions.

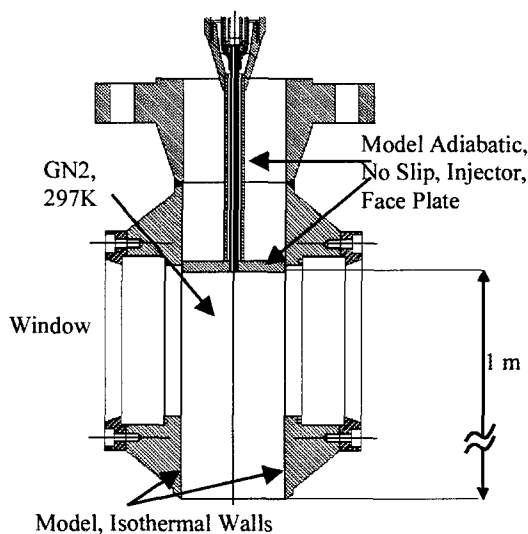


Figure 2: Test chamber

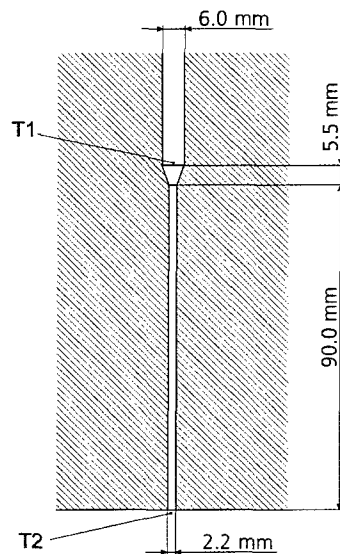


Figure 3: Injector

The Raman and Shadowgraph images taken were processed to produce density, length scales and spreading angles to compare to the modelled test conditions. This procedure is reported in reference 6.

### Modeling

The model for this multi-physical problem bases itself on a straight forward computational approach. The flow field calculations employ directly the Navier-Stokes equations for incompressible flow. Since the test conditions are in the supercritical regime for nitrogen, real gas nitrogen properties are necessary. For this requirement, the model employs the Lee-Kessler<sup>17</sup> and Chung<sup>18</sup> model built into the CFD-ACE software. The model density results were compared to Younglove<sup>19</sup> to ensure accuracy of the input property data. Without high velocity and the use of real gas properties, it is possible to employ the incompressible solution scheme and still take into account the variable density. The model focuses on a steady state solution to determine average property distributions for this injection experiment. The orientation of the injector also allows the assumption of negligible body forces. A look at the calculated Grashof, Froud, and Reynolds numbers for this experimental range shows the inertial forces to be the most significant with buoyancy and viscous forces somewhat less reinforcing this assumption. Therefore, the classical flow equations for this problem are as follows:

Continuity

$$\frac{\partial}{\partial x_j} (\rho u_j) = 0$$

Momentum (Navier-Stokes)

$$\frac{\partial}{\partial x_j} (\rho u_i u_j) = -\frac{\partial P}{\partial x_i} + \frac{\partial}{\partial x_j} \left\{ \mu \frac{\partial u_i}{\partial x_j} + \frac{\partial u_j}{\partial x_i} - \frac{2}{3} \mu \frac{\partial u_k}{\partial x_k} \delta_{ij} \right\}$$

Energy equation

$$\frac{\partial}{\partial x_j} (\rho u_j H) = \frac{\partial}{\partial x_j} \left( K \frac{\partial T}{\partial x_j} \right) + \frac{\partial u_i}{\partial x_i} (\tau_{ij} u_j) - \frac{\partial}{\partial x_j} (J_{ij} h_i)$$

Modeling these equations directly is very difficult and is only practical for simple flow situations. For this reason, the density averaging technique derives a time averaged solution by using an average value and fluctuation to replace actual flow parameter values. This relationship produces a workable equation set called Favre Averaged Navier-Stokes (FANS) and can be found in Cebec and Smith<sup>20</sup> as well as many other texts.

The FANS introduces the Reynolds stresses to account for turbulence in the flow. While several methods exist to estimate these values, the k-ε model seems to be the most appropriate. This method has shown much success in similar problems and reduces calculation times. The model calculations used this high Reynolds approximation in the flow and semi-empirical calculation techniques to determine flow parameters next to the wall. In the boundary layer the viscous forces are much greater than shear forces, Launder and Spalding<sup>21</sup>. The temperature calculation for the heat transfer is treated in a similar manner. The program discretized the governing equations using a third order accurate scheme to capture the large density gradients and damped with first order upwind discretization to maintain stable mathematical computations in the CFD-ACE software package<sup>12</sup>.

The software package takes into account the contribution of heat and mass transfer from the turbulence by use of a turbulent Prandtl and Schmidt number. The heat transfer module solves the total enthalpy form of the energy equation as shown.

$$\nabla \cdot (\rho \vec{v} h_e) = \nabla \cdot (k \nabla T) + \frac{\partial (u \tau_x)}{\partial x}$$

The calculation of an effective conductivity ( $K_{eff}$ ) value takes into account the turbulence effect. The following equation shows how the program uses a turbulent Prandtl number to accomplish this. By using the turbulent Schmidt number, the program handles the mass diffusion in a similar way to calculate an effective diffusion coefficient.

$$K_{eff} = K + \frac{\nu_t \rho c_p}{Pr_t}$$

#### Grid

The computational grid used for this problem is a structured, 2-D, axisymmetric grid with just over 100,000 cells. The refinement in the injector region is critical and can be seen in Figure 4

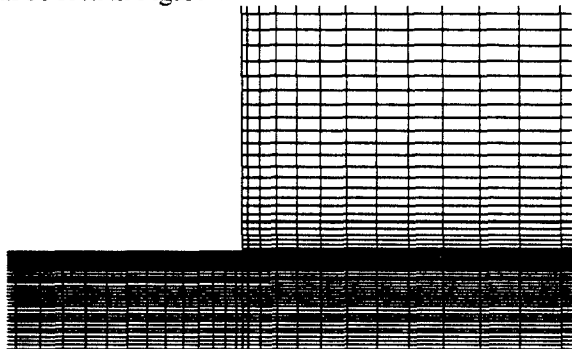


Figure 4: Grid

To show the solution is independent of this grid, the same conditions were calculated for Case 3 using several coarser grids. A grid with 85,000 cells compared well to the solution for the primary grid (100,000 cells). The agreement between the coarser grid and fine grid is very good. The axial density profile exemplifies this agreement (Figure 5). Therefore, the results are considered the same and the solution is independent of both grids. The finer grid was used for all the test conditions to ensure grid independence at the other testing conditions.

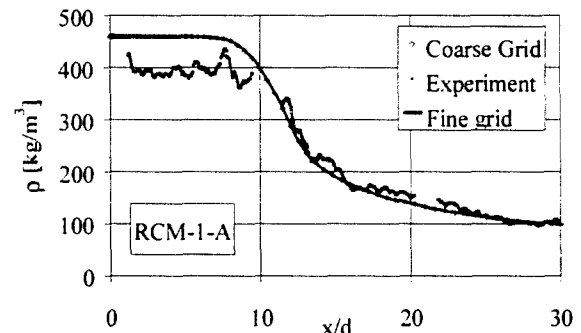


Figure 5: Density, 4 MPa, 5 m/s, 120 K

#### Boundary and Initial Conditions

The inlet and boundary conditions for this model are very important and extremely sensitive to temperature. The experiments include measurements to determine the influence of temperature on the actual temperature and pressure input values for the model. Measured mass flow, temperature and pressure determine the inlet conditions. From the measured values, initial inlet velocity, turbulent kinetic energy ( $k$ ) and rate of dissipation ( $\epsilon$ ) are calculated and input to the model.

$$k = \frac{3}{2} (Iu)^2 \quad \epsilon = \frac{C_{\mu}^{3/4} k^{3/2}}{0.014l}, \quad C_{\mu} = 0.09$$

The Lee-Kessler-Chung real gas properties and measured mass flow for the test condition determine the inlet velocity from the density. For the inlet conditions, inlet velocity and an assumed turbulence intensity (for this model, 5%) determine  $k$ . The length scale ( $l$ ) in the turbulent energy dissipation rate calculation is the inlet diameter (2.2 mm).

The outer wall of the chamber is isothermal to correspond to the character of the wall during testing. The actual test chamber has also shown some heat transfer to the nitrogen in the injector tube. To account for this in the model, the temperature determined at the chamber inlet is used as the injector tube inlet temperature. The boundary conditions used are then an adiabatic wall along the injector tube and the end of the chamber at the plane of injection into the chamber. This allows the temperature into the chamber to match experimentally measured values for these test cases. Also, to take into account turbulence contributions to thermal and momentum energy transfer, the turbulent Prandtl number is set to 1.0. This value corresponds to Reynolds contention of turbulent-momentum flux and heat flux being of the same order of magnitude (White<sup>13</sup>).

The model procedures calculate the outlet boundary condition based on total mass flow. The chamber is long

enough to consider the exit to be completely decoupled from the jet flow. Extrapolated calculations for the outlet did not take into account the mass flow being entrained in the jet from the chamber and therefore gave erroneous velocity. By establishing exit velocity as a fixed value, the calculations could account for this problem and smoothly resolve the jet flow realistically. The initial conditions for the calculations are simply set to the outlet boundary conditions, low velocity at ambient temperature and chamber pressure, Figure 2.

### Convergence

The models went through between 20,000 to 30,000 iterations for the various test cases in order to ensure convergence of the solution. Several are similar to previously run test conditions and used these final solutions as the initial conditions therefore requiring fewer iterations to converge. A mass flow balance performed by the program provides final proof of convergence. The difference between mass inflow and mass outflow show values more than five orders of magnitude smaller than total mass flow into the chamber. During the iterations, the procedure required the models to stop and mass flow calculations were performed to ensure proper inlet velocity values were being used. The inlet velocity was adjusted as appropriate and the result was 0.00% to 0.12 % variance between model calculated mass flow and measured mass flow.

### Results

The comparison of the various effects on the injection of liquid nitrogen includes density and velocity profile comparisons. Experimental data (Raman and Shadowgraph images) provide us with information on density profiles, divergence angles and length scales to compare to our model results as well.

### Density Profiles

When looking at the progression of the calculated density profiles from  $x/d = 1.2$  to  $x/d = 25$ , the graphs show the development of the flow as it moves toward a self similar solution. Figure 6 from RCM-1-A exhibits this trend seen at these testing conditions. The profiles closer to the injector show a flat region ( $\rho^* = 1.0$ ) near the center line ( $r/r_{1/2} = 0$ ) which eventually no longer exists at  $x/d \geq 10$ . This corresponds to the potential core. Even though some of the testing cases show little potential core in the measured data, the models calculated core lengths for each testing condition. This results from the quality of the Raman images. The Shadowgraph images show a definite potential core in these regions and provide some validity to the model results.

The transition from a liquid-like jet behavior through the transition region to a fully gas-like jet behavior can be easily seen in the profile after  $r/r_{1/2} = 1.0$ . Following the progression of the jet using the density profiles from  $x/d = 1.2$  to  $x/d = 10$ , the slope progressively increases. For the profile at  $x/d = 15$ , the slope has again dramatically decreased and the profiles after this axial location continue to decrease slightly and converge. The profiles for  $x/d = 20$  and 25 very nearly share the same line. The experimental data has a considerable amount of variability

(no error bars are shown for clarity) but follows the trend of the computational models.

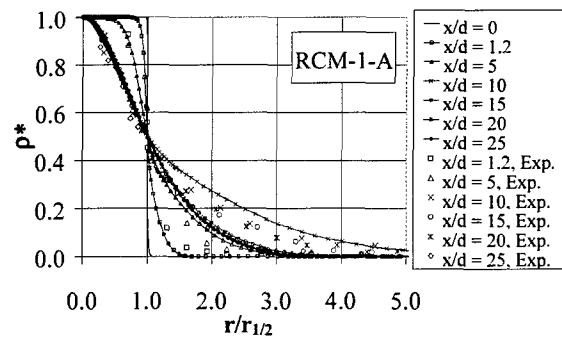


Figure 6: Density; 4 MPa, 5 m/s, 120 K

Figure 7 shows another way to easily see the trend for the jet to move through the transition region and to the self similar region quickly. This figure presents density profiles ( $\rho^*$ ) as a function of  $r/x$ , RCM-1-B.

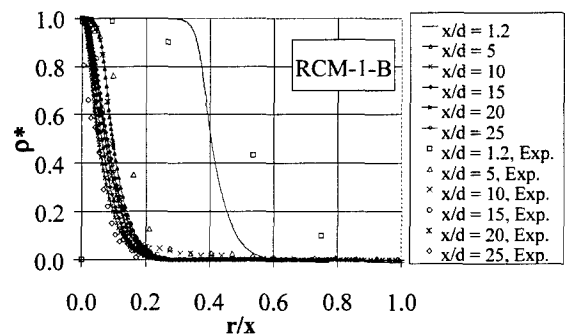


Figure 7: Density; 6 MPa, 5 m/s, 120 K

The effect of using axial position to normalize the profile radial position shifts the profiles very near the injector to the right and dramatically portrays the expected potential core ( $x/d = 1.2$ ). As the profiles are plotted at intervals away from the injector, the density properties show similar behavior as seen in Figure 6. The slope for the entire profile increases until  $x/d = 10$  and then begins to decrease again. This is opposite to the behavior in Figure 6 due to the method of presenting the data but corresponds to the same phenomena. The jet has a high density core to an axial position near  $x/d = 10$ , it then goes through a turbulent transition and then begins to develop into a self similar jet flow. Figure 7 also shows the profiles at  $x/d = 20$  and 25 do not collapse to the same line, therefore the relationship suggests the flow has not yet reached self similarity. The experimental data corresponds with this trend again. At  $x/d = 1.2$ , the very sensitive nature of using axial position to present radial profiles at locations very near the injector causes the difference between the model and experimental data.

In looking at the agreement of the density determined from the Raman images and the calculated model, Figure 8 shows a representative sample of a profile at  $x/d = 20$  for RCM-1-A. The experimental deviation was calculated from the values used to get an average density at each location. This difference is a product of the averaging technique and the variability of the data. This figure shows a good agreement with the experimental values.

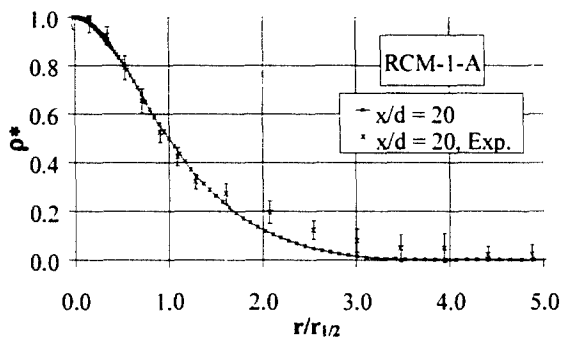


Figure 8: Density; 4 MPa, 5 m/s, 120 K

### Velocity Profiles

The velocity profiles in the radial direction lend themselves to portraying jet development from the injection point to a fully developed condition better than density. With the flow inertially dominated, the expectation would be to see the velocity profiles developing rather quickly into self similar relationships. Figure 9, RCM-1-B shows the initial velocity to be a fully developed, turbulent pipe flow profile. It develops into a fairly self similar profile very quickly by  $x/d = 20$  and 25. These profiles show the edge of the jet to be near  $r/r_{1/2} \approx 2.5$ .

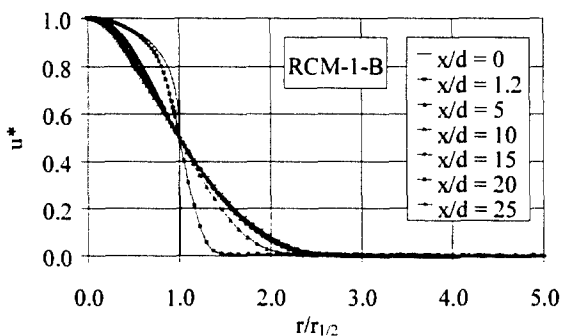


Figure 9: Velocity; 6 MPa, 5 m/s, 120 K

The velocity profiles of the flow develop much faster than temperature or density distributions for these modeled conditions. Figure 10 from RCM-1-A shows a typical representation of the velocity profiles as well. By  $x/d = 10$ , the jet appears to be nearly self similar although the jet is not fully developed as seen from the density profiles.

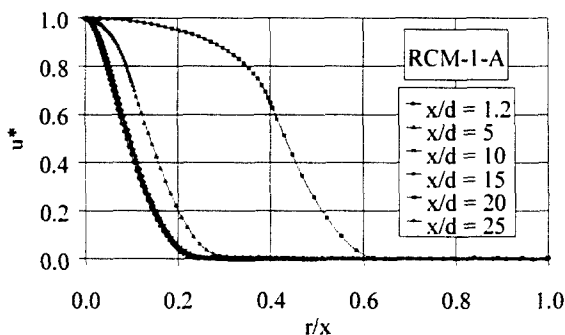


Figure 10: Velocity; 4 MPa, 5 m/s, 120 K

### Centerline Density

The centerline density calculations prove to be useful in looking at several aspects of the jet. Primarily, this axial

property relationship shows how the jet dissipates with distance from the injector. Observations of the axial density profile provide insight into the behavior of the jet as it moves through the various stages of a jet development. The experimental data also provides a means to compare the computational results with actual testing conditions. In Figure 11 Case 4, the computational results present a correlation with the experimental data, even though variability in experimental data makes it difficult to obtain exact agreement. If the temperature is below the peak in specific heat, the jet is very dense needing more energy to increase the temperature. Beyond this peak, the density ratio of ambient gas to injected fluid is higher than closer to the injector and the jet dissipates rapidly.

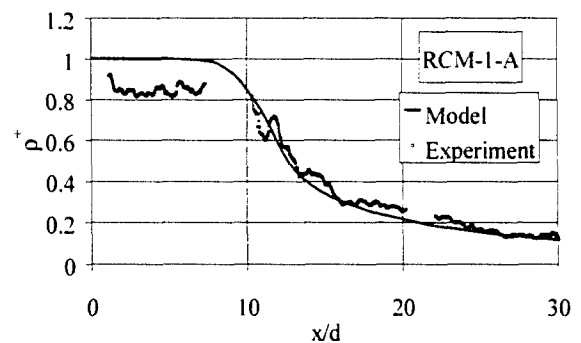


Figure 11: Density; 4 MPa, 5 m/s, 120 K

From Figure 11, the expected characteristics of the potential core are very obvious with the density ratio approximately constant until  $x/d \approx 8$ . At this point, the density falls off fairly quickly but does not reach ambient values until much further downstream ( $x/d > 100$ ). These profiles provide insight into the development of the jet through the various regions when viewed on a logarithmic scale as seen from Figure 12; the potential core, transition region and fully developed region.

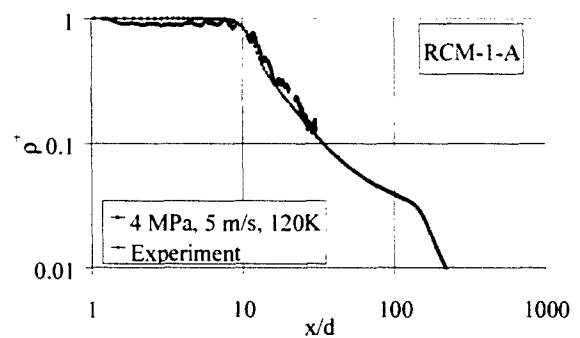


Figure 12: Density; 4 MPa, 5 m/s, 120 K

Figure 12 shows the behavior of a jet (RCM-1-A) with a very dense core, the transition to a turbulent mixing zone and then into a fully developed region. The steep slope at  $x/d = 10$  to approximately  $x/d = 30$  shows the rapid transfer of both momentum and thermal energy. At this point in the jet flow, the density gradient is lower and the dissipation is also reduced suggesting a region of developed flow. At a point past  $x/d = 150$ , the density falls off quickly toward the chamber value suggesting the jet has almost completely dissipated. The model calculations show this location in the chamber to be the far edged of a recirculation zone established to transfer mass back to-

ward the injector. This mass is the mass entrained in the jet flow from the chamber.

### Liquid Core Length

The centerline density is a power function of the axial distance from the injector. When plotted on a log-log scale, it is much easier to determine liquid core length and see the various regions of the jet. The location where the density begins to drop off rapidly determines the liquid core length ( $x_c/d$ ). This location is easily seen in Figure 12. For these test campaigns, several other conditions were also tested and calculated. These testing conditions provide information at various density ratios. Figure 13 shows the comparison of these testing conditions for values of core length obtained from the calculated models against the Reynolds number relationship from Harsha and the relationship offered by Chehroudi. The two lines identify the range Chehroudi gave for the coefficient in his relationship. The calculated values agree better with the empirical gas relationship suggested by Harsha but tend to fall at or below the lower limit suggested by Chehroudi. The agreement of the core length calculations to a gas jet suggests the cryogenic jet under supercritical pressure behaves very similar to a gas jet.

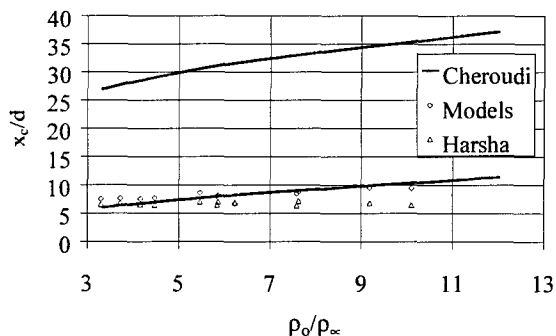


Figure 13: Core Length

Unfortunately, it is difficult to determine highly reliable values for the core length from the Raman and Shadowgraph images. Another observation of the relationship for the core length is the values appeared to be nearly linear over the range of Reynolds numbers and density ratios for these experiments.

### Angle of Jet Divergence, $\alpha$

The angle of jet divergence is determined from different methods. The computational models used two primary methods and applied each to velocity, temperature, and density. The first one uses the FWHM values and determines the spreading angle from these radial locations. As suggested by Chehroudi et al<sup>14</sup>, the values are then multiplied by 2. The second one looks at the 99% roll-off point to determine the jet width. The computational models allow this point to be determined quite easily

The results show a considerable difference between the 50% method and the 99% values. When considering the possibility the FWHM location doesn't correspond to half of the jet width, another value for the 2x factor can be calculated. For velocity and temperature, this factor is approximately 2.5 which corresponds nicely with the radial profiles when using  $r_{1/2}$  to normalize the radial

distance. In Figure 9, the profiles, beginning to show a self similar behavior, converge at  $r/r_{1/2} \approx 2.5$  for the edge of the jet ( $u^* \approx 0.0$ ). The relationship for the density is the same. In Figure 6, the profiles converge to an  $r/r_{1/2} \approx 3.0$  and the value calculated from the model numbers is the same. This result can then be compared to the difference in the Raman and Shadowgraph methods since both techniques result from density relationships. The Raman images lend themselves to determining the FWHM values easier than finding the edge of the jet, while the Shadowgraphs show the edge of the jet fairly clearly.

From the Raman data, the FWHM difference between centerline and ambient density determines the jet spreading angle. Close to the injector exit, the centerline density is quite high and the jet is quite compact. Added to this, the temperature difference across the shear layer is small compared with the difference across the entire jet. The dense core of the jet therefore determines the FWHM instead of the shear layer. Therefore, the angle is small close to the injector when determined in the region  $x/d \approx 0$  to 10.

In the images for  $x/d \approx 10$  to 20 and 20 to 30, the jet warms up and dissipates. The centerline density is of the same order of magnitude as the density in the shear layer. Therefore, the FWHM location falls within the shear layer. Comparison with the computational results shows a fairly good agreement, Figure 14. For the coldest cases, the angles based on the FWHM are very small or even negative near the injector. For RCM-1-A, the minimum value for  $r_{1/2}/d$  corresponds with the potential core length ( $x_c/d = 9.52$ ). The conclusion then is the growth rate of the shear layer and the radial distance of the injected fluid moving away from the jet does not correspond to the angle measured from Raman data when the centerline density is significantly higher than the density in the shear layer and ambient gas (the region near the injector).

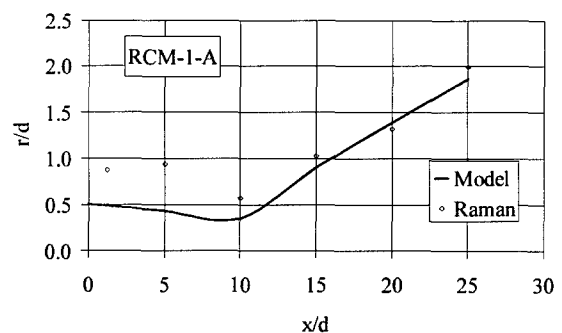


Figure 14: Density FWHM; 4 MPa, 5 m/s, 120 K

Looking at the computational model results and comparing them with the Shadowgraph values shows a slightly under-predicted trend. In the Shadowgraph images, regions are visible where the fluid is in turbulent motion causing local density gradients. The boundary of these regions at the quiescent ambient gas determines the jet spreading angle. A comparison to the angle from numerical calculations using the 99% roll-off point of the velocity shows good agreement.

Figure 15 shows how the models for various density ratios, Raman images and Shadowgraph images compare

with the relationships put forth by Dimotakis<sup>15</sup> and Papamoschou and Roshko<sup>16</sup>. Shadowgraph data was also added from testing conditions using an injector with  $l/d = 11.3$  at sub- and supercritical conditions. The model calculations seem to agree fairly well with the Dimotakis relationship in this density ratio region. The variability of the averaged Raman data is fairly apparent in this figure. Even though there is also some variability in the Shadowgraph data, a relationship with the Dimotakis curve also seems apparent.

Data from earlier experiments is also included in Figure 15. The experiments at low density ratios ( $\rho_\infty/\rho_0$ ) show a significant influence of the Reynolds number. The Reynolds number depends on the increasing of the injection velocity. Correspondingly, the aerodynamic forces also and are sufficient to dissipate the jet. At increased density ratios, the jet dissipates even at low injection velocity and the Reynolds number has only a weak influence on the jet spreading angle.

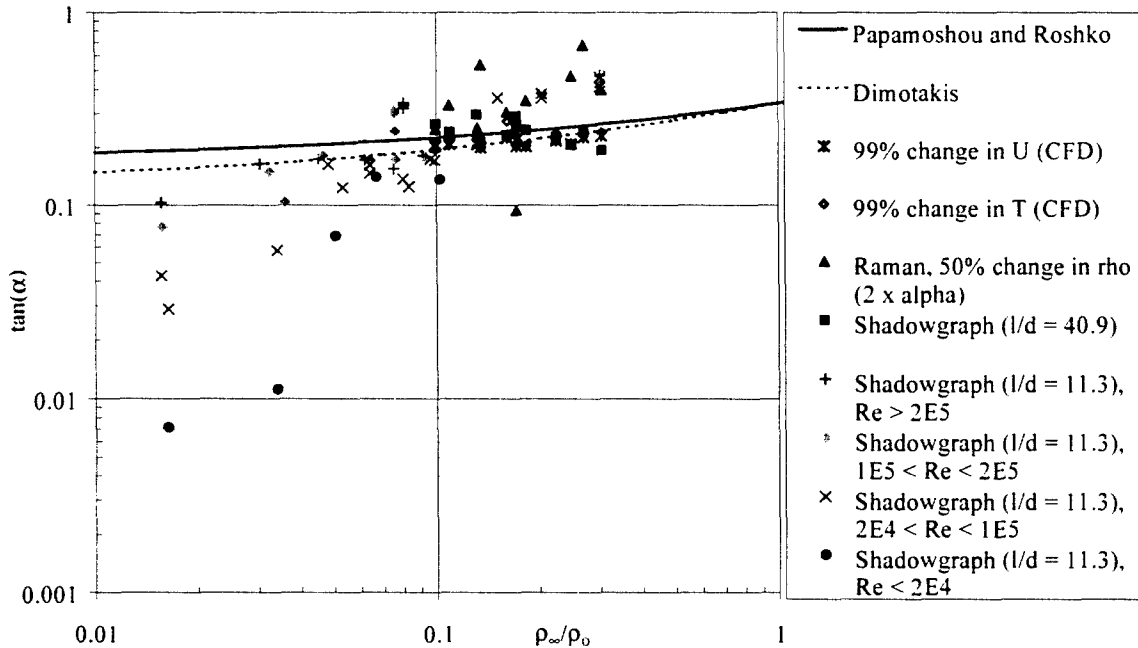


Figure 15: Jet Divergence Angle,

### Length Scales

The Kolmogorov and Integral length scales are:

$$L_{kol} = \left[ \frac{\nu^3}{\epsilon} \right]^{1/4} \quad L_{int} = \frac{k^{3/2}}{\epsilon}$$

These values are highly dependent on the eddy viscosity method used for these calculations to model turbulence. The computational models calculated these values over the entire profile of the jet. At  $x/d = 5$  (Figure 16, RCM-1-B), minimum values for the integral length scale ( $L_{int}$ ) occur at the edge of the potential core flow and then again at the edge of the shear layer. The later location of  $r/d \approx 1.4$  corresponds to the edge of the jet based on 99% change for temperature and velocity.

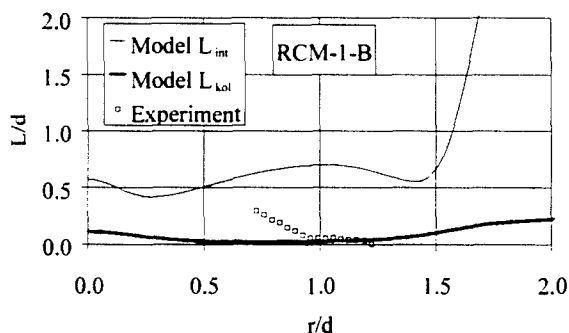


Figure 16:  $L_{int}$ ,  $L_{kol}$  at  $x/d = 5$ ; 6MPa, 5 m/s, 120 K

The Kolmogorov length scales tend to be slightly higher in the potential flow region and somewhat constant throughout the shear layer. Outside the shear layer, both length scales increase dramatically due to the chamber temperature but have little physical significance to the actual jet flow itself.

Figure 17 for RCM-1-B exemplifies a typical length scale comparison at  $x/d = 10$ . Since all cases show core lengths at approximately this location, the expectation would be no or little evidence of the first minimum in the integral length scale as seen in Figure 16. However, the graph shows some evidence of a potential core region. The reason is in this region the flow is in a high state of transition to a purely gas like jet flow. The second minimum at  $r/d \approx 2.5$  corresponds to the values calculated for the edge of the jet using temperature and velocity.

In both cases (Figure 16 and Figure 17), the geometric mean length scale determined from the Shadowgraphs shows a remarkably good comparison with the Kolmogorov length scale. Since these scales are the smallest expected eddies in the flow, these results are expected for a visual measuring technique. Measuring the integral length scales using this method is not possible since these structures also include all of the easier seen smaller length scales as well. The length scales closer to the center of the flow ( $r/d = 0$ ) appear to increase slightly. For the colder flow fields ( $T = 120$  K), the use of the Shadowgraph

images and the higher density gradients in this region cause the calculation technique to give larger values for the length scales near the centerline.

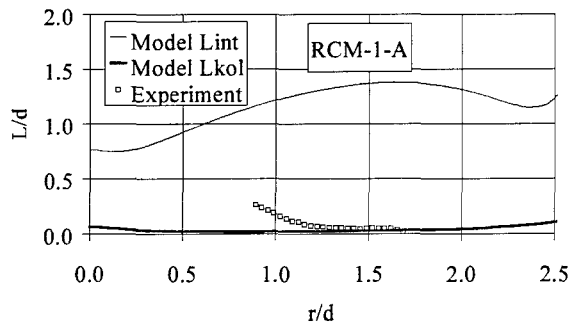


Figure 17:  $L_{int}$ ,  $L_{kol}$  at  $x/d = 10$ ; 4MPa, 5 m/s, 120 K

### Turbulent Prandtl Number

The comparison of the results of two different turbulent Prandtl numbers for RCM-1-A, Figure 18 shows the better relationship for  $Pr_T = 1.0$  when considering our experimental data for density. This data is comprised of three individual zones ( $x/d$  0..10, 10..20, and 20..30 approximately). While the first region suggests a significant difference between the model and the measured data, the following two regions corresponded nicely with the model.

Since the relationship of the momentum and thermal energy dissipation defines the turbulent Prandtl number, a value of one would cause the velocity and temperature profiles to be very similar when non-dimensionalized. For values of turbulent Prandtl number less than one as in Figure 18, the similarity between the non-dimensional temperature and velocity would be less pronounced. Our experimental data compares better with an axial density profile when using  $Pr_T = 1.0$ . This suggests the turbulent momentum transfer is as important in explaining the state of the jet as turbulent thermal energy transfer as suggested by Reynolds (White<sup>13</sup>).

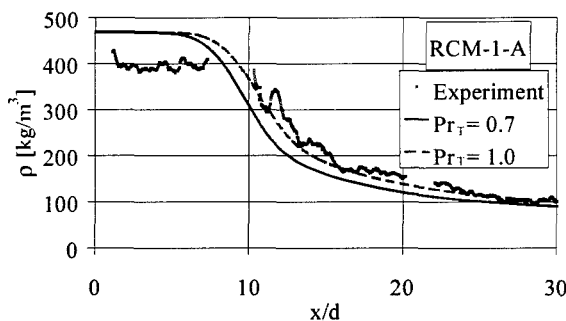


Figure 18: Density, 4 MPa, 5 m/s, 120 K

### Pressure Influence

The different pressure conditions in the flow (4 and 6 MPa) show little impact on the behavior of the cryogenic jet since these pressure conditions are constant for the chamber and are all above the critical pressure of nitrogen (3.39 MPa). Figure 19 shows the axial density profile for Case 3 and Case 11, 120 K and 5 m/s. The Reynolds numbers and density ratios are very similar meaning the only significant difference is the pressure. The difference in temperature at the injector ( $T_2$ ) causes the slight variation between the two cases (Case 3, 126.9 and Case 11,

128.7K). At values so near the critical temperature of 126.2, this small variation influences the density significantly.

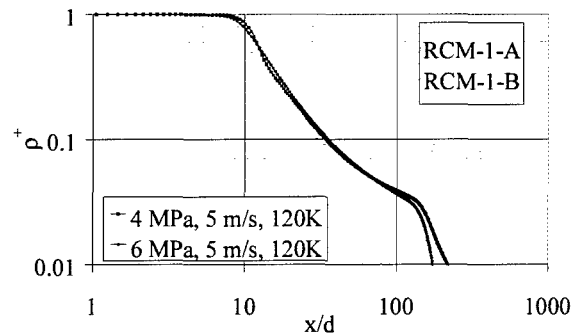


Figure 19: Density; 5 m/s, 120 K

The influence on the velocity field due to pressure differences also proves to be difficult to determine. Since the temperature and velocity values between the various test conditions vary somewhat (i.e. RCM-1-A,  $T = 126.9$  K at  $u_{ave} = 5.72$  m/s and RCM-1-B,  $T = 128.7$  K at  $u_{ave} = 5.40$  m/s), it is difficult to say the influence is only due to the pressure difference.

### Conclusions

Understanding the complex phenomena of a supercritical injection flow field still requires a considerable amount of research, but this work provides some insights into several aspects of a rocket injector. This work accomplished this by examining a single injector using liquid nitrogen above the critical pressure. The various testing conditions considered pressures from 4 to 6 MPa at two target velocities (2 and 5 m/s) and a target injection temperatures of 120 K. The experimental data compares well with numerical results from these testing conditions. Agreement of the numerical results with density, length scales and jet spreading angles obtained from Raman and Shadowgraph images quantitatively validates them.

Under these testing conditions, the velocity and density profiles show a distinct trend toward a self similar jet flow as early as  $x/d = 25$ . The centerline density profiles in the axial direction provide considerable insight into the jet development from initial core length through to the dissipation of the jet. The core lengths determined from the computational models agree fairly well with the Harsha gas jet empirical approximation and appear to be fairly constant over this density ratio and Reynolds number range. Mass fraction profiles show the importance of the coefficient of specific heat, specifically in RCM-1-A. When injecting fluid below the critical temperature as well as above the critical pressure, as the jet warms up, it will reach the temperature at which  $c_p$  reaches a maximum value. The heat transfer from the surrounding gas to the colder jet at this temperature has a dramatically higher transfer rate at this location in the jet. The flow conditions and specifically density seem to be most affected by inlet temperature variations at temperatures so close to the critical point.

The various methods for determining the spreading angle proves useful for comparison, but values from the numerical models determined from a 99% roll off point for velocity agree best with the measured Shadowgraph val-

ues and the Dimotakis model. From the spreading rate analysis, a further conclusion reached is the growth rate of the shear layer and the radial distance injected fluid moves away from the jet has no significant influence on the angle measured from Raman data when the centerline density is significantly higher than the density in the shear layer and the ambient gas. This result is apparent from the FWHM method of determining the spreading angle from the Raman images. The resulting angles do not correspond with the Shadowgraph or the numerical results very well. The procedure of multiplying the FWHM values by a factor of 2 also does not prove to be very accurate when applied to the numerical results.

### Acknowledgements

This work is supported by the Federal Ministry of Education and Research (BMBF) under contract number 50TT9627 (Project TEKAN). The project was accomplished in the frame of the SPP, 'Atomization and Spray Processes' under the guidance of DFG (Deutsche Forschungsgemeinschaft).

### Nomenclature

$C, C_\mu$	Constants
$c_p$	Coefficient of specific heat constant pressure
$d$	Injector diameter (2.2 mm)
$g$	Universal gas constant
$h, H$	Enthalpy
$J$	Momentum
$k$	Turbulent kinetic energy
$k_T$	Eddy conductivity
$k_{eff}$	Effective kinetic turbulent energy
$K$	Thermal conductivity
$L_{int}$	Integral length scale
$L_{kol}$	Kolmogorov length scale
$Pr_T$	Turbulent Prandtl number
$r$	Radial location
$r_{1/2}$	Radial location of half maximum value of a parameter
$T$	Temperature
$u$	Axial velocity
$u', v', w'$	Turbulence intensity values
$x$	Axial location
$Y$	Mass fraction
$\alpha$	Jet divergence angle
$\delta_\omega'$	Vorticity growth rate (radians)
$\epsilon$	Turbulent energy rate of dissipation, optical efficiency
$\kappa$	Thermal conductivity
$\nu$	Kinematic viscosity
$\nu_T$	Turbulent eddy viscosity
$\rho$	Density, number density
$\tau$	Shear stress
Sub- and Super-scripts	
ax	Axial direction
c	Centerline value at specified axial location
i, j, k	x, y and z, Cartesian directions
o	Centerline value at the injector
rad	Radial direction
T	Turbulent parameter

$\infty$	Chamber property away from the jet
*, +	Dimensionless values
'	Fluctuation from the mean value

### References

1. Mayer, W. and Tamura, H., "Propellant Injection in a Liquid Oxygen/Gaseous Hydrogen Rocket Engine," J. of Propulsion and Power, Vol. 12, No.6, pp. 1137 - 1147, 1996.
2. Ivancic, B.; Mayer, W.; Krülle, G.; Brüggemann, D., "Experimental and Numerical Investigation of Time and Length Scales in LOX/GH2-Rocket Combustors," 35th Joint Propulsion Conference, AIAA 99-2211, Los Angeles, June 20-24, 1999.
3. Mayer, W.; Schik, A.; Schäffler, M.; Tamura, H., "Injection and Mixing Processes in High-Pressure Liquid Oxygen/Gaseous Hydrogen Rocket Combustors," J. of Propulsion and Power, Vol. 16, No. 5, pp. 823-828, 2000
4. Mayer, W., "TEKAN - Research on Cryogenic Rocket Engines at DLR Lampoldshausen," 36th Joint Propulsion Conference, AIAA 2000-3219, Huntsville, July 16-19, 2000.
5. Mayer, W.; Schik, A.; Vieille, B.; Chaveau, C.; Goekalp, I.; Talley, D.; Woodward, R. "Atomization and Breakup of Cryogenic Propellants under High-Pressure Subcritical and Supercritical Conditions," J. of Propulsion and Power, Vol. 14, No. 5, pp. 835-842, 1998
6. Mayer, W.; Telaar, J.; Branam, R.; Schneider, G.; Hussong, J. "Characterization of Cryogenic Injection at Supercritical Pressure," 37th Joint Propulsion Conference, AIAA 2001-3275, Salt Lake City, July 9-11, 2001.
7. Schetz, J. A., Injection and Mixing in Turbulent Flow, Progress in Aeronautics and Astronautics, Vol 68, AIAA 1980, pp. 19-84.
8. Schlichting, H. Boundary-Layer Theory, McGraw Hill, New York, 1979, pp. 729-755.
9. Pabst, O., "Die Ausbreitung heisser Gasstrahlen in bewegter Luft, I Teil-Versuche in Kerngebiet," *Deutsche Luftfahrtforschung*, Aug. 1944.
10. Sakipov, Y.B. and Temirbaev, D.J., "On the Ratio of the Coefficients of Turbulent Exchange of Mass and Heat in a Free Turbulent Jet," *Tepli i Massoperenos*, Vol. 2, 1965, pp. 407-413.
11. Wilcox, D.C., Turbulence Modeling for CFD, DCW Industries, La Canada, CA, 1994, pps.181-2.
12. CFD-GUI5TM User manuals, CFD Research Corporation; Huntsville, AL, October 1998, pg. 3-13.
13. White, F.M. Viscous Fluid Flow, McGraw Hill, Inc. New York, 2nd Edition, 1991, pg. 482.
14. Chehroudi B.; Cohn, R.; Talley, D.; and Badakhshan A., "Raman Scattering Measurements in the Initial Region of Sub- and Supercritical Jets," 36th Joint Propulsion Conference, AIAA 2000-3392, Huntsville, July 14-19, 2000.

- 
15. Dimotakis, P.E., "Two-dimensional Shear-layer Entrainment," AIAA Journal, vol. 24, no. 11, Nov. 1986, pp. 1791-1796.
  16. Papamoschou, D. and Roshko, A. "The Compressible Turbulent Shear Layer: an Experimental Study," J. Fluid Mech., vol. 197, 1988, pp. 453-477.
  17. Lee, B.I. and Kesler, M.G., "A Generalized Thermodynamic Correlation Based on Three-Parameter Corresponding States," AIChE J., Vol. 21, p. 510, May 1975.
  18. Chung et al., "Generalized Multiparameter Correlation for Nonpolar and Polar Fluid Transport Properties," Ind. Eng. Chem. Res., Vol. 27, p. 671, 1988.
  19. Younglove, B.A. Thermophysical Properties of Fluids. Journal of Physical Chemistry, Reference Data 11: Supplement 1.
  20. Cebec, T. and Smith A.M.O. Analysis of Turbulent Boundary Layers. Academic Press, New York, 1974.
  21. Launder, B.E. and Spalding, D.B., "Computational Methods Applied Mechanical Engineering", vol. 3, 1974.